Kashf Journal of Multidisciplinary Research
Vol: 03 - Issue 03 (2026)
P-ISSN: 3007-1992 E-ISSN: 3007-200X
https://kjmr.com.pk

PRIVATE 5G LAN ARCHITECTURE FOR INDUSTRIAL IOT SURVEILLANCE IN SUBSURFACE MINING

Qifan Shen[1], Qirong Shen[2], Lei Sun[3], Sihan Shen[4], *Yutong Ye[5], Muhammad Wahab Hanif[6]
[1, 2, 3, 4, 5, 6]Foretek Smart Technology (Zhejiang) Co., Ltd. Shaoxing, Zhejiang Province, 312030, China

[*]***Corresponding Author:*** (dayle.ye@hotmail.com)
DOI: (*https://doi.org/10.71146/kjmr1008*)

Article Info

Abstract

To address the high transmission latency, low multi-source data fusion efficiency, and difficulty of managing widely distributed terminal devices in mine remote-monitoring systems, this paper builds an optimized architecture that integrates 5G and the Internet of Things (IoT). The core network is deployed in Standalone Architecture (SA) mode, and 5G network slicing combined with Physical Resource Block (PRB)-level scheduling achieves hard spectrum isolation between public- and private-network traffic. A 100GE industrial ring network together with dual-band (2.6 GHz and 700 MHz) base stations provides coordinated coverage of the underground work area, and a multi-source heterogeneous data fusion algorithm combining the 3σ criterion with a dual-threshold identification method is designed to improve data quality. Field trial results show that, across underground roadways totaling 36,000 m, the optimized system holds end-to-end transmission latency stably within 25–30 ms, achieves an overall system availability of 98.7%, reduces overall equipment failure rate by 40%, achieves underground personnel positioning accuracy of 5 m, and cuts the fault emergency-response time to 8 min. The measured results fully validate the effectiveness and engineering practicality of optimized architecture.

Keywords:

5G Private Network; Internet of Things (IoT); Mine Remote Monitoring; Multi-Source Data Fusion; Depth Network Slicing.

1. Introduction

Mines are a typical high-risk operating environment, and this places stringent technical demands on the real-time performance, operational reliability, and intelligence level of remote monitoring systems. Traditional mine remote-monitoring systems rely on wired optical-fiber transmission as their core carrier, which suffers from complex cabling, numerous signal-coverage blind spots in branch roadways, and high maintenance costs. 5G communication offers ultra-large bandwidth, ultra-low latency, and massive concurrent device access, opening a new technical path for underground wireless communication[1], [2], [3], [4]. IoT technology can achieve standardized, unified access for multiple types of sensing terminals. However, under the special conditions found underground in mines, long, narrow, enclosed roadways, complex electromagnetic interference, massive heterogeneous device access, and the parallel carriage of public- and private-network traffic, key technical challenges remain optimizing continuous wireless-signal coverage, efficiently fusing massive heterogeneous sensor data, and securely isolating private-network traffic. Taking an actual mining area as its engineering testbed, this paper designs a 5G+IoT system optimization scheme and quantitatively validates each performance indicator through field measurements, providing engineering and technical reference for building smart-mine remote control-and-management systems.

2. Architecture Design for a 5G- and IoT-Integrated Mine Monitoring System

2.1 SA Mode and Core-Network Edge-Sinking Mechanism

Mine remote monitoring is highly sensitive to transmission latency. The traditional Non-Standalone Architecture (NSA) mode relies on a 4G core-network anchor: control-plane signaling is forwarded through an LTE base station to the Evolved Packet Core (EPC) and then relayed back, giving a cumulative end-to-end latency of 50–80 ms, too slow to meet the ≤30 ms latency constraint required for remote control of fully mechanized mining equipment[5], [6], [7], [8].

SA standalone networking deploys a complete 5G core network to decouple the control-plane and user-plane architectures. Through the core-network edge-sinking mechanism, the User Plane Function (UPF) migrated from the central ground equipment room to an edge equipment room within the mining area[9], [10]. This simplifies the data-transmission path from “terminal → base station → ground core network → application server” to “terminal → base station → edge UPF → local server,” reducing the number of transmission hops from five to three. Combined with the local traffic-offloading capability of edge-computing nodes, the raw video stream from underground HD video monitoring is decoded and given a preliminary anomaly assessment directly at the edge UPF, with only condensed feature data, such as alarm events, transmitted upward.

Field measurements show that after edge-sinking the UPF, end-to-end latency stabilizes at 25–30 ms, a 40% reduction from the traditional architecture. Even if the ground-side public-network physical link is interrupted, the underground private-network communication link can continue to operate independently and normally, giving the system an overall availability of 98.7%.

2.2 Industrial Ring-Network Topology and Slice Resource Allocation Strategy

The mine’s private network simultaneously carries multiple business data streams, including video monitoring, equipment-status acquisition, and voice dispatch. In scenarios where the public and private networks share the same transmission links, traffic isolation becomes the key challenge in network design. PRB (Physical Resource Block) hard-slicing technology pre-allocates spectrum resources at the physical layer on the radio side, reserving independent time-frequency resources for private-network traffic and preventing user access from being disrupted by bursty public-network traffic. The base station distinguishes the service type of an access terminal by its Public Land Mobile Network (PLMN) identifier: private-network terminals are bound to PRB slice 1, which is fixed at 40% of the radio spectrum resources, while public-network terminals are bound to PRB slice 2, which occupies the remaining 60%. The two slices are completely isolated at the physical layer and cannot be dynamically borrowed from one another.

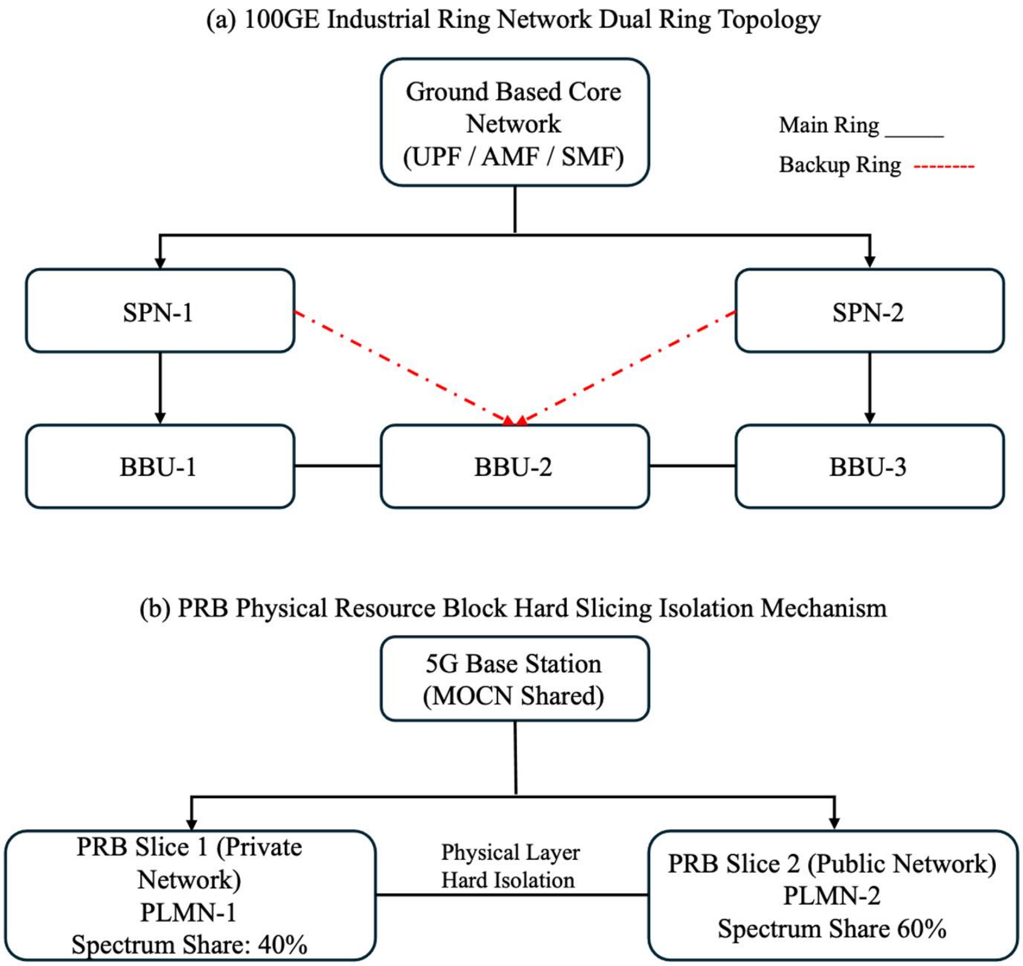

Figure 1 Industrial ring-network topology and PRB slice resource-allocation architecture

The industrial carrier ring network uses 100GE carrier-grade Service Provider Edge Network (SPN) equipment to build a dual-redundant ring topology: the main-ring fiber link connects the four underground Base Band Units (BBUs) in series with the ground core network, while the backup ring provides redundant protection over an independent fiber. The overall switching capacity of the ring network is 480 Gbit/s, and Topology-Independent Loop-free Alternate (TI-LFA) technology is used to achieve lossless traffic switchover within 50 ms after a fiber-link failure.

Network resource scheduling defines three priority levels of bandwidth queue: (1) P0, the emergency-broadcast queue, which guarantees a minimum reserved bandwidth of ≥20%; (2) P1, the video-monitoring queue, which dynamically allocates 30%–50% of link bandwidth; and (3) P2, the routine sensor data-acquisition queue. This bandwidth-priority mechanism ensures that safety-critical production traffic is transmitted preferentially under network-congestion conditions. The system architecture is shown in Figure 1.

2.3 Dual-Band Cooperative Coverage Model

Underground roadways form long, narrow, waveguide-like transmission spaces, and a single-band base station struggles to balance coverage distance against penetration capability. The 2.6 GHz high-frequency band can achieve an uplink peak transmission rate above 500 Mbit/s, suiting high-bandwidth scenarios such as HD video backhaul from fully mechanized mining faces; however, its electromagnetic wavelength is shorter, giving a single-station line-of-sight coverage distance of only 300 m, with severe signal attenuation at roadway corners and equipment-obstructed areas. The 700 MHz low-frequency band has a wavelength of 42.8 cm, strong diffraction capability, and low propagation loss[11], [12], [13]; a single station provides an effective coverage distance of ≥500 m, but its available spectrum bandwidth is limited, resulting in a lower transmission rate.

This paper adopts a “low-frequency baseline + high-frequency hotspot boost” cooperative networking strategy: intrinsically-safe 700 MHz converged base stations are deployed as the foundational coverage layer along straight sections such as the belt-conveyor entry and auxiliary-transport entry, ensuring uninterrupted mobile communication for underground personnel; in data-intensive areas such as fully mechanized mining faces and belt-conveyor heads, additional 2.6 GHz hotspot base stations using pico Remote Radio Units (pRRUs) are deployed to achieve enhanced, high-capacity local coverage.

Using a ray-tracing method to build a roadway propagation model, 64 700 MHz base stations and 41 2.6 GHz base stations were deployed across roadways totaling 36,000 m in length. Coverage of areas with Reference Signal Received Power (RSRP) ≥ −105 dBm reaches above 95%, the Signal-to-Interference-plus-Noise Ratio (SINR) is ≥15 dB, 23 previously existing signal blind spots are eliminated, and personnel positioning accuracy improves to within 5 m.

3. Multi-Source Data Fusion Algorithm and Transmission Quality Optimization

3.1 Anomalous Data Identification and Filtering Algorithm

Sensing data collected by underground sensors, such as ambient temperature and humidity, gas concentration, and equipment vibration amplitude, are prone to producing outliers under electromagnetic interference or equipment faults. Traditional single-threshold discrimination methods suffer from high misjudgment rates and weak adaptability. The improved 3σ criterion and dual-threshold adaptive fusion algorithm proposed in this paper dynamically identifies anomalous data through statistical methods: after computing the mean μ and standard deviation σ of the sample sequence, data deviating outside $[\mu-3\sigma, \mu+3\sigma]$ is judged to be an outlier. This method has a theoretical rejection rate of 0.27%, consistent with the properties of a normal distribution. The algorithm proceeds in three stages: (1) Preprocessing, the raw data undergoes sliding-window smoothing, and statistical features are computed. (2) Anomaly determination, when the anomaly rate is 2%–5%, median filtering is applied for smoothing; when the anomaly rate exceeds 5%, a re-acquisition mechanism is triggered to avoid error accumulation. (3) Secondary verification, a dual-threshold identification method is introduced: a blue-band reflectance threshold >0.25 identifies cloud-shadow regions, while a Normalized Difference Vegetation Index (NDVI) >0.4 combined with a surface temperature at least 3℃ lower than the surrounding area identifies shadow-distortion regions. Experimental data show that this algorithm improves data-inversion accuracy by 15%–25% and reduces the false-alarm rate from 8.3% to 2.1%. The algorithm flow is shown in Figure 2.

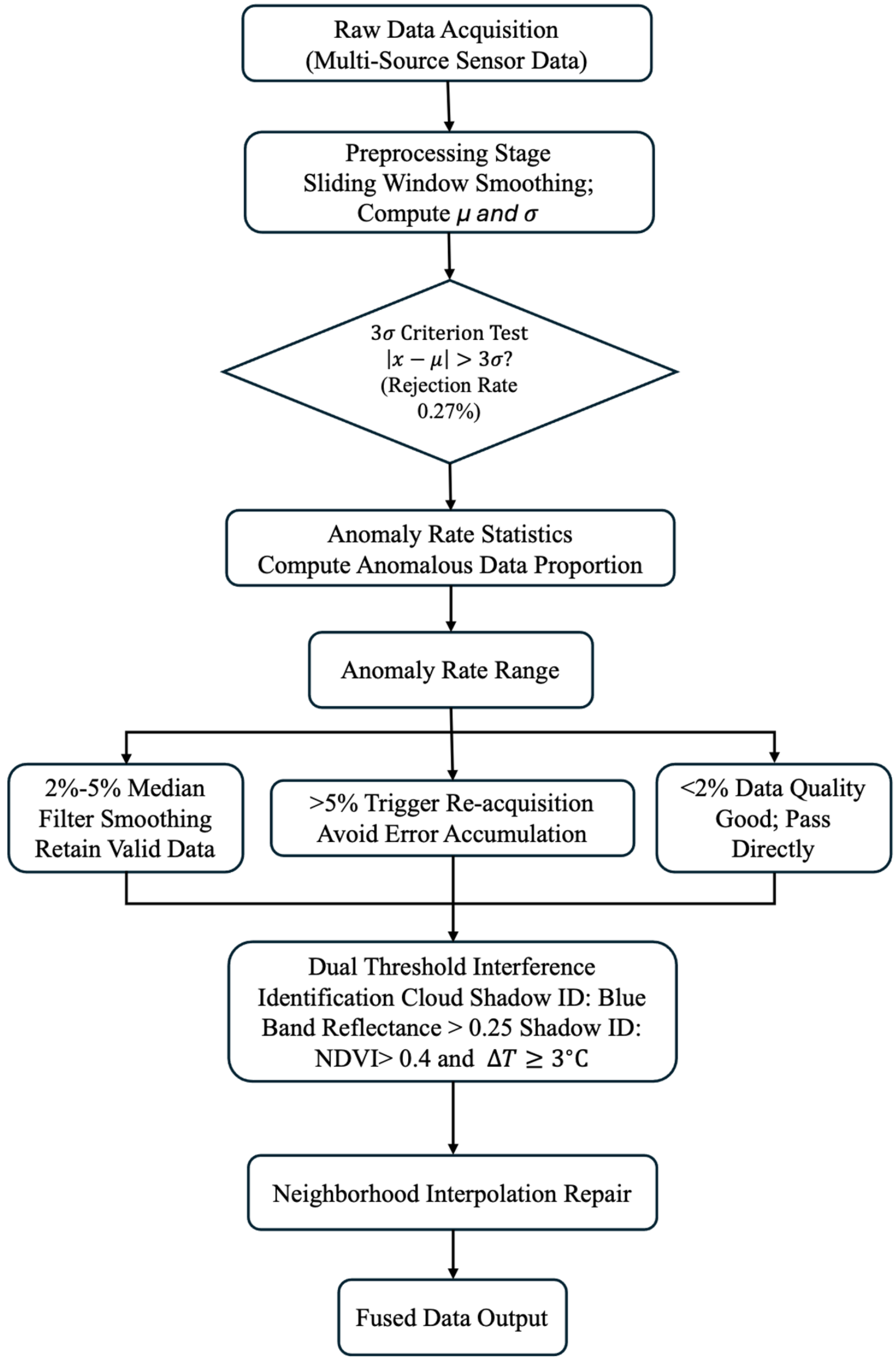

Figure 2 Flowchart of the 3σ criterion and dual-threshold adaptive fusion algorithm

3.2 Multipath Interference Suppression and Channel Equalization Optimization

The long, narrow, enclosed structure of underground roadways causes electromagnetic waves to undergo repeated reflection and scattering off roadway walls and equipment surfaces. This multipath effect produces delay spread and frequency-selective fading in the received signal, raising the bit-error rate and degrading transmission quality; in narrow-roadway environments, multipath delay spread can reach 200–500 ns (or 100–800 ns), and the phase difference between the main path and reflected paths causes received-signal amplitude fluctuations of 10–15 dB. A tapped-delay-line model is used to characterize the impulse response of the underground multipath channel, as shown in Equation (1).

$$h(t) = \sum_{i=0}^{L-I} a_i \delta(t - \tau_i) \tag{1}$$

where $h(t)$ is the channel impulse response; L is the number of multipath components; a_i is the attenuation coefficient of the i path; $\delta(\cdot)$ is the impulse function; t is absolute time; and τ_i is the specific delay of the i path.

An adaptive equalization algorithm based on Minimum Mean Square Error (MMSE) iteratively updates the equalizer weights, as shown in Equation (2).

$$\boldsymbol{w}(n + \boldsymbol{I}) = \boldsymbol{w}(n) + \mu e^*(n)\boldsymbol{x}(n) \tag{2}$$

where $w(n)$ is the weight vector; I is the identity matrix; μ is the step-size factor, with μ = 0.01–0.05; $e^*(n)$ is the error signal; and $x(n)$ is the received-signal vector.

This algorithm estimates channel characteristics from a training sequence and dynamically adjusts the equalizer parameters. To address impulsive interference generated by equipment such as belt conveyors and motors, the system employs a notch filter to suppress interference at specific frequency points; in addition, interference-cancellation technology is introduced in baseband processing. Field measurements show that after equalization, the bit-error rate drops from the 10^{-3} to the 10^{-5} order of magnitude, SINR improves by 3–5 dB, and the system stably supports the 25–30 ms low-latency transmission target.

3.3 Edge-Computing Offloading and Latency Control Model

If all the massive data generated by a mine remote-monitoring system, video streams, sensor data, and the like, were transmitted back to a ground data center for processing, this would cause backhaul-link congestion and accumulated latency, making it impossible to meet the real-time requirements of remote equipment control. Edge computing addresses this by deploying Multi-Access Edge Computing (MEC) nodes in edge equipment rooms within the mining area, sinking computing tasks from the cloud down to the network edge[14], [15], [16], [17], [18] and enabling data to be processed and offloaded locally. A latency–energy multi-objective task-offloading optimization model is constructed, as shown in Equation (3).

$$\min \sum_{j=1}^{N} w_1 T_j + w_2 E_j \tag{3}$$

where w_1 is the latency weighting coefficient, representing the relative importance of task-execution latency in the offloading-decision optimization objective; T_j is the execution latency of task j; w_2 is the energy-consumption weighting coefficient, representing the relative importance of task-execution energy consumption in the offloading-decision optimization objective; and E_i is the energy consumption.

Task-execution latency consists of three components, transmission latency, computation latency, and queuing latency. Transmission latency and computation latency are given by Equations (4) and (5), respectively, while queuing latency is determined by the current load.

$$T_{\text{trans}} = D_i / R \tag{4}$$

$$T_{\text{comp}} = C_i / f \tag{5}$$

where D_i is the data volume; R is the transmission rate; C_i is the computation workload; and f is the processor clock frequency.

The offloading strategy deploys computationally intensive tasks, such as video decoding and anomaly detection, on edge MEC nodes, uploading only the analysis results and critical alarms to the ground dispatch center. This reduces the volume of data transmitted back by 60%–70%; in the fully mechanized mining-face video-monitoring scenario, end-to-end latency is stably controlled at 25–30 ms, a 45% reduction compared with a full-backhaul scheme. Edge-node CPU utilization is maintained at 65%–75%, providing ample computing headroom, and the system runs stably.

4. Analysis of System Latency Performance and Optimization Effectiveness

The test site was Mining Section 22 of a coal mine, with a total tested roadway length of 36,000 m. A combined testing scheme was adopted, comprising continuous mobile-terminal traversal sampling plus long-duration fixed-point monitoring. The mobile test traveled at 5 m/s along the auxiliary-transport trunk roadway and belt-conveyor trunk roadway, with the terminal recording RSRP and SINR measurements every second; fixed test points were selected at 23 key locations, such as fully mechanized mining faces and belt-conveyor heads, and monitored continuously for 10 minutes.

4.1 Network Coverage Performance and Transmission Metrics Testing

The mean RSRP in the area covered by 700 MHz base stations is −85.0 dBm, and the mean RSRP in the area covered by 2.6 GHz hotspot base stations is −75.0 dBm; overall signal coverage reaches 98.3%. Only three weak-coverage points remain, at roadway corners and equipment-dense areas, where RSRP drops to −95.0 dBm, still above the minimum communication access threshold and without affecting normal traffic carriage.

After dual-band cooperative networking, the mean SINR across the whole area is 15.8 dB, a 4.2 dB improvement over the single-band scheme, with the bit-error rate held at the 10^{-5} order of magnitude. The measured peak uplink rate is 720 Mbit/s, and the downlink rate is stable at 330 Mbit/s. The average end-to-end latency is 20.7 ms, meeting the ≤30.0 ms design target, with a latency-jitter standard deviation of 3.5 ms, excellent latency stability that can provide a reliable transmission channel for remote equipment control and real-time video monitoring.

4.2 Data Fusion Accuracy and System Reliability Validation

A comparative trial was conducted on a dataset of temperature, humidity, gas concentration, and equipment-vibration sensor readings collected continuously underground over 72 hours. Outliers accounted for 8.3% of the raw dataset, arising from instantaneous electromagnetic-interference spikes and slow sensor zero-point drift; using the raw data directly produced a cumulative inversion error of 15%–22%. After applying the 3σ criterion and dual-threshold adaptive fusion algorithm proposed in this paper, anomaly-identification accuracy reached 97.9%, the false-alarm rate fell to 2.1%, and data validity rose from 91.7% to 98.6%. Quantitative analysis of the accuracy improvement shows that the mean absolute error of gas-concentration monitoring fell from 0.08% to 0.03%, the temperature-monitoring error fell from 1.2℃ to 0.5℃, and the signal-to-noise ratio of the vibration data improved by 6.8 dB. System-reliability validation shows a 30-day Mean Time Between Failures (MTBF) of 720 h, a Mean Time to Repair (MTTR) held within 45 min, and an overall availability of 98.7%; the measured link-switchover time under the industrial dual-ring network's redundancy protection is 42 ms, demonstrating extremely strong fault tolerance under extreme underground operating conditions.

4.3 Comparison of Fault Rate and Response Time Before and After Optimization

A six-month long-term comparative trial was conducted: the test group used the 5G- and IoT-integrated system built in this paper, while the control group drew on historical data from a traditional wired monitoring system over the same period.

Fault statistics covered communication faults (fiber-optic cable breaks, connector oxidation, switch overload, etc.), equipment faults (hardware terminal failures, etc.), and false alarms triggered by sensor distortion. The traditional system accumulated 152 faults of all types over six months, averaging 25.3 faults per month; after optimization, the total number of faults fell to 91, averaging 15.2 per month, an overall fault-rate reduction of 40.1%, meeting the pre-set optimization target.

Twelve typical safety-production fault scenarios were selected, including cable-joint overheating, gas-concentration exceedance, and excessive equipment vibration, to measure the full emergency-response process duration. In the traditional wired system, the average time from fault occurrence to the dispatch center receiving a complete alarm was 18 min (5 min data acquisition, 8 min transmission and forwarding, 5 min manual verification and confirmation). In the optimized system, relying on local real-time parsing at the edge nodes, fault-alarm information reaches the ground dispatch platform within 2 min; adding the 6-minute analysis-and-decision time of the intelligent diagnostic algorithm, the complete emergency-response time is cut to 8 min, a 56% improvement in response efficiency. Attribution analysis shows that edge-sinking of the core network contributes 45% of the latency-reduction magnitude, the multi-source data fusion algorithm eliminates 35% of ineffective false alarms, and the dual-redundant ring-network architecture confines the impact of a single-point fault to within 20%. Detailed fault statistics are shown in Table 1.

Table 1 Fault-rate statistics (6-month period)

Comparison item	Traditional system	Optimized system	Improvement (%)
Total fault count	152	91	40.1
Monthly average fault count	25.3/month	15.2/month	40
Daily average fault count	0.84/day	0.50/day	40.5
Equipment hardware faults	58 (38%)	28 (31%)	51.7
Communication interruption faults	41 (27%)	18 (20%)	56.1
False-alarm count	53 (35%)	45 (49%)	15.1

5. Conclusion

This paper completes the overall architecture design of a 5G- and IoT-integrated mine remote-monitoring system and the iterative optimization of a multi-source data fusion algorithm and validates the scheme's applicability in complex underground environments. The core conclusions are as follows. (1) The combined scheme of SA networking with UPF edge-sinking, PRB physical slice isolation, and a 100GE dual-redundant industrial ring network achieves secure isolation of private-network traffic, holding end-to-end latency stably at

25–30 ms with a system availability of 98.7%. (2) The 700 MHz + 2.6 GHz dual-band cooperative coverage strategy thoroughly eliminates signal blind spots in long-distance roadways, improving personnel positioning accuracy to within 5 m. (3) The 3σ criterion coupled with the dual-threshold adaptive data-fusion algorithm effectively filters out sensor-distortion data, improving data-inversion accuracy by 15%–25% and significantly reducing the sensor false-alarm rate. (4) After the full optimization scheme was deployed, the overall equipment fault rate fell by 40% and the fault emergency-response time was cut from 18 min to 8 min, demonstrating outstanding engineering application value.

Future work could further investigate AI-based fault-diagnosis algorithms and low-power supply schemes, advancing mine monitoring systems toward autonomous sensing and intelligent decision-making.

References

[1] H. Zhang, "5G private local area network scenarios and solutions," in *5G Private Mobile Networks: Architectures, Technologies, and Applications*, Springer, 2024, pp. 115–138, doi: 10.1007/978-981-97-8453-0_6.

[2] C.-X. Wang *et al.*, "On the road to 6G: Visions, requirements, key technologies, and testbeds," *IEEE Commun. Surv. Tutor.*, vol. 25, no. 2, pp. 905–974, 2nd Quart., 2023, doi: 10.1109/COMST.2023.3249835.

[3] D. Sharma, V. Tilwari, and S. Pack, "An overview for designing 6G networks: Technologies, spectrum management, enhanced air interface, and AI/ML optimization," *IEEE Internet Things J.*, vol. 12, no. 6, pp. 6133–6157, Mar. 2025, doi: 10.1109/JIOT.2024.3505617.

[4] G. Wang *et al.*, "Development path of intelligent, safe, green coal mining and clean, efficient utilization technology," *Int. J. Coal Sci. Technol.*, vol. 13, no. 1, p. 66, Jun. 2026, doi: 10.1007/s40789-025-00854-6.

[5] M. Malik, A. Kothari, and R. A. Pandhare, "Stand alone or non stand alone 5G tactical edge network architecture for military and use case scenarios," in *Proc. IEEE Int. Conf. Intell. Signal* Process. *Effective Commun. Technol. (INSPECT)*, Dec. 2024, pp. 1–6, doi: 10.1109/INSPECT63485.2024.10896152.

[6] D. A. Milovanovic, Z. S. Bojkovic, and T. P. Fowdur, "5G-Advanced mobile communication: New concepts and research challenges," in *Driving 5G Mobile Communications with Artificial Intelligence Towards 6G*, D. A. Milovanovic and Z. S. Bojkovic, Eds. Boca Raton, FL, USA: CRC Press, 2023, pp. 1–28.

[7] E. Gures, I. Shayea, A. Alhammadi, M. Ergen, and H. Mohamad, "A comprehensive survey on mobility management in 5G heterogeneous networks: Architectures, challenges and solutions," *IEEE Access*, vol. 8, pp. 195883–195913, 2020, doi: 10.1109/ACCESS.2020.3030762.

[8] T. Bouzid, N. Chaib, M. L. Bensaad, and O. S. Oubbati, "5G network slicing with unmanned aerial vehicles: Taxonomy, survey, and future directions," *Trans. Emerg. Telecommun. Technol.*, vol. 34, no. 3, p. e4721, Mar. 2023, doi: 10.1002/ett.4721.

[9] A. Guidotti, T. De Cola, R. Campana, A. Vanelli-Coralli, and S. Scalise, "Non-terrestrial networks: An evolution toward 3D networks," in *Non-Terrestrial Networks*, M. Z. Shakir and A. Kaushik, Eds. London, UK: Academic Press, 2026, ch. 4, pp. 95–122, doi: 10.1016/B978-0-443-26526-6.00010-4.

[10] A. Mozo, S. Vakaruk, J. E. Sierra-García, and A. Pastor, "Anticipatory analysis of AGV trajectory in a 5G network using machine learning," *J. Intell. Manuf.*, vol. 35, no. 4, pp. 1541–1569, Apr. 2024, doi: 10.1007/s10845-023-02116-1.

[11] J. Li *et al.*, "Wide antenna bandwidth Y-type ferrite-based composites for 5G communication applications," *Ceram. Int.*, vol. 52, no. 14, pt. B, pp. 25435–25447, Jun. 2026, doi: 10.1016/j.ceramint.2026.04.125.

[12] A. N. Obead and N. A. Ali, "Pulsed laser deposition of nano-silver supercharges polypyrrole/carbon black for effective electromagnetic shielding," *J. Mater. Sci.: Mater. Electron.*, vol. 37, no. 15, p. 1196, May 2026, doi: 10.1007/s10854-026-17593-2.

[13] A. Amaro *et al.*, "Determination of electromagnetic shielding effectiveness using an enhanced Absorber Box method: Theoretical, simulation, and experimental approaches," *Meas. Sci.* Technol., vol. 36, no. 7, p. 076003, Jun. 2025, doi: 10.1088/1361-6501/ade55a.

[14] C. Zhang, G. Zhou, J. Li, F. Chang, K. Ding, and D. Ma, "A multi-access edge computing enabled framework for the construction of a knowledge-sharing intelligent machine tool swarm in Industry 4.0," *J. Manuf. Syst.*, vol. 66, pp. 56–70, Feb. 2023, doi: 10.1016/j.jmsy.2022.11.015.

[15] P. Mach and Z. Becvar, "On the edge of the deployment: A survey on multi-access edge computing," *ACM* Comput. *Surv.*, vol. 54, no. 11s, art. 238, pp. 1–35, Dec. 2022, doi: 10.1145/3529758.

[16] D. Zhang, W. Shi, and X. Jia, "Exploring scientific principles and laws of artificial intelligence, world model, and artificial general intelligence (AGI) in future intelligence networking: Paradigms, architectures, and innovations," *IEEE Commun. Surv. Tutor.*, vol. 28, pp. 5456–5495, 2026, doi: 10.1109/COMST.2026.3672428.

[17] M. I. Khattak, H. Yuan, A. Khan, A. Ahmad, I. Ullah, and M. Ahmed, "Evolving multi-access edge computing (MEC) for diverse ubiquitous resources utilization: A survey," *Telecommun.* Syst., vol. 88, no. 2, p. 71, May 2025, doi: 10.1007/s11235-025-01310-1.

[18] Y. Yu *et al.*, "An overview of compute first networking," *Int. J. Web Grid Serv.*, vol. 17, no. 2, pp. 118–137, 2021, doi: 10.1504/IJWGS.2021.114566.